

# Constraints on decaying Dark Matter from *XMM-Newton* observations of M31

Alexey Boyarsky<sup>a,b</sup>, Dmytro Iakubovskiy<sup>b</sup>, Oleg Ruchayskiy<sup>c</sup>, and Vladimir Savchenko<sup>b,d</sup>

<sup>a</sup>*PH-TH, CERN, CH-1211 Geneva 23, Switzerland*

<sup>b</sup>*Bogolyubov Institute for Theoretical Physics, Kiev 03780, Ukraine*

<sup>c</sup>*École Polytechnique Fédérale de Lausanne, Institute of Theoretical Physics, FSB/ITP/LPPC, BSP 720, CH-1015, Lausanne, Switzerland*

<sup>d</sup>*Physics Department, Kiev National Taras Shevchenko University, Kiev 03022, Ukraine*

Received <date> ; in original form <date>

## ABSTRACT

We derive constraints on the parameters of the radiatively decaying Dark Matter (DM) particle, using the *XMM-Newton* EPIC spectra of the Andromeda galaxy (M31). Using the observations of the outer ( $5'$ - $13'$ ) parts of M31, we improve the existing constraints. For the case of sterile neutrino DM, combining our constraints with the latest computation of abundances of sterile neutrinos in the Dodelson-Widrow (DW) scenario, we obtain the lower mass limit  $m_s < 4$  keV, which is stronger than the previous one  $m_s < 6$  keV, obtained recently by Asaka et al. (2007). Comparing this limit with the most recent results on Lyman- $\alpha$  forest analysis of Viel et al. (2007) ( $m_s > 5.6$  keV), we argue that the scenario in which all the DM is produced via the DW mechanism is ruled out. We discuss however other production mechanisms and note that the sterile neutrino remains a viable candidate for Dark Matter, either warm or cold.

## 1 INTRODUCTION

A vast body of evidence points to the existence of Dark Matter (DM) in addition to the ordinary visible matter in the Universe. The evidence includes: velocity curves of galaxies in clusters and stars in galaxies; observations of galaxy clusters in X-rays; gravitational lensing data; cosmic microwave background anisotropies. While the DM contributes some 22% to the total energy density in the Universe, its properties remain largely unknown.

The Standard Model of particle physics (SM) does not provide a DM candidate. The DM cannot be made out of baryons, as such an amount of baryonic matter cannot be generated in the framework of an otherwise successful scenario of Big Bang nucleosynthesis (Dar 1995). In addition, current microlensing experiments exclude the possibility that MACHOs (massive compact halo objects) constitute the dominant amount of the total mass density in the local halo (Gates et al. 1995; Lasserre et al. 2000; Alcock et al. 2000). The only possible non-baryonic DM candidate in the SM could be the neutrino, however this possibility is ruled out by the present data on the large scale structure (LSS) of the Universe.

What properties of the DM particles can be deduced from existing observations? Some information comes from studies of structure formation. Namely, the velocity distribution of the DM particles at the time of structure formation affects greatly the power spectrum of density perturbations, as measured by a variety of experiments (see e.g. Tegmark et al. 2004). One of the parameters, characterizing the influence of the DM velocity dispersion on the power spectrum, is the *free-streaming length*  $\lambda_{FS}$  – the distance traveled by the DM particle from the time when it became non-relativistic until today. Roughly speaking, the free-streaming length determines the minimal scale at which the Jeans instability can develop, and therefore non-trivial free-streaming implies modifi-

cation of the spectrum of density perturbations at wave numbers  $k \gtrsim \lambda_{FS}^{-1}$ .

If the DM particles have negligible velocity dispersion, they constitute the so-called *cold* DM (CDM), which forms structure in a “bottom-up” fashion (i.e. smaller scale objects formed first and then merged into the larger ones, see e.g. Peebles 1980). The neutrino DM represents the opposite case – *hot* DM (HDM). In HDM scenarios, structure forms in a top-down fashion (Zel’dovich 1970), and the first structures to collapse have size comparable to the Hubble scale (Bisnovatyi-Kogan 1980; Bond et al. 1980; Doroshkevich et al. 1981; Bond & Szalay 1983). In this scenario the galaxies do not have enough time to form, contradicting to the existing observations (see e.g. White et al. 1983; Peebles 1984).

*Warm* DM (WDM) represents an intermediate case, cutting structure formation at some scale, with the details being dependent on a particular WDM model.

Both WDM and CDM fit the LSS data equally well. The differences appear when one starts to analyze the details of structure formation for galaxy-size objects (modifications of the power spectrum at momenta  $k \gtrsim 0.5h\text{Mpc}^{-1}$ ). It is usually said that WDM predicts “less power at smaller scales”, meaning in particular that one expects smaller number of dwarf satellite galaxies and shallower density profiles than those predicted by CDM models (Navarro et al. 1997; Klypin et al. 1999; Ghigna et al. 2000). Thus WDM models can provide the way to solve the “missing satellite” problem and the problem of central density peaks in galaxy-sized DM halos (Klypin et al. 1999; Moore et al. 1999; Bode et al. 2001; Avila-Reese et al. 2001).

There exist a number of direct astrophysical observations which seem to contradict the N-body simulations of galaxy formations, performed in the framework of the CDM models (e.g. Diemand et al. 2007; Strigari et al. 2007). Namely, direct mea-

measurements of the DM density profiles in dwarf spheroidal (dSph) satellites of the Milky Way favour cored profiles (Gilmore et al. 2006, 2007; Wu 2007; Gilmore 2007).<sup>1</sup> The number of dwarf satellite galaxies, as currently observed, is still more than an order of magnitude below the CDM predictions, in spite of the drastically improved sensitivity towards the search (see Gilmore et al. 2007; Kopolov et al. 2007) and resolution of numerical simulations (Strigari et al. 2007). There seems to exist a smallest scale ( $\sim 120$  pc) at which the DM is observed (Gilmore et al. 2007; Gilmore 2007). However, as of now there is no definitive statement about the “CDM substructure crisis” (see Simon & Geha (2007) in regard to the smallest observed DM scale and Penarrubia et al. (2007) for an alternative solution of the “missing satellite problem”).

The power-spectrum of density perturbations at scales of interest for the WDM vs. CDM issue can also be studied, analyzing the Lyman- $\alpha$  forest data (absorption feature by the neutral hydrogen at  $\lambda = 1216\text{\AA}$  at different red-shifts in the distant quasar spectra, Hui et al. 1997). This involves comparison of the observed spectra of Ly- $\alpha$  absorption lines with those obtained as a result of numerical simulations in various DM models. In this way one arrives at an upper limit on the free-streaming length of the DM particles.

Various particle physics models provide WDM candidates. Possible examples include gravitinos and axinos in various supersymmetric models (see e.g. Baltz & Murayama 2003; Cembranos et al. 2006; Seto & Yamaguchi 2007). Another WDM candidate is the sterile neutrino with a mass in the keV range (Dodelson & Widrow 1994). Recently, this candidate received a lot of attention. Namely, an extension of the minimal SM (MSM) with the three right-handed neutrinos was suggested (Asaka & Shaposhnikov 2005; Asaka et al. 2005). This extension (called  $\nu$ MSM) explains several *observed* phenomena beyond the MSM under the minimal number of assumptions. Namely, apart from the absence of the DM candidate, the MSM fails to explain observed *neutrino oscillations* – the transition between neutrinos of different flavors (for a review see e.g. Fogli et al. 2006; Strumia & Visani 2006; Giunti 2007). The explanation of this phenomenon is the existence of neutrino mass. The most natural way to provide this mass is to add right-handed neutrinos. Indeed, in the MSM, neutrinos are left-handed (all other fermions have both left-handed and right-handed counterparts) and strictly massless. The structure of the MSM dictates that right-handed neutrinos, if added to the theory, would not be charged with respect to any Standard Model interactions and interact with other matter only via mixing with the usual (left-handed) neutrinos (that is why right-handed neutrinos are often called *sterile neutrinos* to distinguish them from the left-handed *active* ones). Moreover, as demonstrated by Asaka & Shaposhnikov 2005, the parameters of added right-handed neutrinos can be chosen in such a way that such a model resolves another problem of the MSM – it explains the excess of baryons over antibaryons in the Universe (the *baryon asymmetry*), while at the same time it does not spoil the predictions of Big Bang nucleosynthesis. For this to be true, the masses of two of these sterile neutrinos should be chosen in the range  $300 \text{ MeV} \lesssim M_{2,3} \lesssim 20 \text{ GeV}$ , while the mass of the third (lighter) sterile neutrino is arbitrary (as long as it is below  $M_{2,3}$ ). In particular, its mass can be in the keV range, providing the WDM candidate. Such a sterile neutrino can

be produced in the Early Universe in the correct amount via various mechanisms: via non-resonant oscillations with active neutrinos (Dodelson & Widrow 1994; Dolgov & Hansen 2002; Abazajian et al. 2001; Asaka et al. 2006, 2007), via interaction with the inflaton (Shaposhnikov & Tkachev 2006), via resonant oscillations in the presence of lepton asymmetries (Shi & Fuller 1999), and have cosmologically long life-time.

Finally, the sterile neutrino with mass in the keV range would have other interesting astrophysical applications (see e.g. Sommer-Larsen & Dolgov (2001); Kusenko (2006); Biermann & Kusenko (2006); Hidaka & Fuller (2006); Hidaka & Fuller (2007); Stasielak et al. (2007) and references therein).

### *Existing bounds on sterile neutrino DM*

The mass of the sterile neutrino DM should satisfy the universal Tremaine-Gunn lower bound (Tremaine & Gunn 1979; Dalcanton & Hogan 2001):  $m_s \geq 300 - 500 \text{ eV}$ . A stronger (although model dependent) lower bound comes from the Lyman- $\alpha$  forest analysis. Assuming a particular velocity distribution of the sterile neutrino<sup>2</sup> one can obtain a relation between the DM mass and  $\lambda_{FS}$  and therefore convert an upper bound on the free-streaming length to a *lower* bound on the mass of the sterile neutrino. In the recent works of Seljak et al. (2006); Viel et al. (2006) this bound was found to be 14 keV (correspondingly 10 keV) at 95% CL in the Dodelson-Widrow (DW) production model (Dodelson & Widrow 1994). New results from QSO lensing give similar restrictions for the DW model:  $m_s \geq 10 \text{ keV}$  (Miranda & Macciò 2007). For different models of production, the relation between the DM mass and the free-streaming length is different and the Lyman- $\alpha$  mass bound for sterile neutrinos can be as low as  $M_s > 2.5 \text{ keV}$  (see e.g. Ruchayskiy 2007).<sup>3</sup>

The sterile neutrino DM is not completely stable. In particular, it has a radiative decay channel into an active neutrino and a photon, emitting a monoenergetic photon with energy  $E_\gamma = m_s/2$  (where  $m_s$  is the mass of the sterile neutrino). As a result, the (indirect) search for the DM decay line in the X-ray spectra of objects with large DM overdensity becomes an important way to restrict the parameters (mass and decay width) of sterile neutrino DM. During the last two years a number of papers appeared devoted to this task: Boyarsky et al. 2006b,c,d,e,a; Riemer-Sørensen et al. 2006; Watson et al. 2006; Boyarsky et al. 2007; Abazajian et al. 2007. The current status of these observations is summarized, e.g., in Ruchayskiy (2007). The results of the computation of sterile neutrino production in the early Universe (Asaka et al. 2007), combined with these X-ray bounds, puts an upper bound on the sterile neutrino mass of  $m_s < 6 \text{ keV}$  (Asaka et al. 2007). This is below the *lower* bound on the sterile neutrino DM mass from the Lyman- $\alpha$  forest analysis of Seljak et al. (2006); Viel et al. (2006). Thus it would seem that the scenario, in which all the sterile neutrino DM is produced via the DW mechanism, is ruled out (the recent work by Palazzo et al. (2007) also explored the possibility that the sterile neutrino, produced through DW scenario, constitutes but a fraction of DM and

<sup>1</sup> For certain dSph cusped profiles are still admissible, but disfavored. Additional considerations rule out the possibility of existence of cusped profiles for the Ursa Minor and Fornax (Kleyna et al. 2003a,b; Goerdt et al. 2006; Sánchez-Salcedo et al. 2006).

<sup>2</sup> Sterile neutrinos are not in thermal equilibrium in the early Universe and therefore their velocity distribution is non-universal and depends on the model of production.

<sup>3</sup> Strictly speaking, in case of other models of production the power spectrum of density fluctuations is not only characterized by the free-streaming length. Therefore, the rescaling of the results of Seljak et al. (2006); Viel et al. (2006) can be used only as the estimates and the reanalysis of the Lyman- $\alpha$  data for the case of each model is required.

found this fraction to be below 70%). However, the results of Seljak et al. (2006); Viel et al. (2006) are based on the low-resolution SDSS Lyman- $\alpha$  dataset of McDonald et al. (2006). It was shown recently by Viel et al. (2007) that using high-resolution HIRES spectra (Becker et al. 2007) one arrives at the lower limit  $m_s > 5.6$  keV. Thus, the small window of masses  $5.6 \text{ keV} < m_s < 6 \text{ keV}$  remains open in the DW model. Therefore further improvement of X-ray bounds is crucial for exploring (and possibly closing) this region of parameters.

It was shown in Boyarsky et al. (2006d) that the objects in the Local Halo (e.g. dwarf spheroidal galaxies) are the best objects in terms of the signal to noise ratio. The Andromeda galaxy (M31) is one of the nearest galaxies, excluding dwarves, that enables one to resolve most of its bright point sources and extract the spectrum of its diffuse emission. It also has a massive and well-studied dark matter halo (e.g. Klypin et al. 2002; Widrow & Dubinski 2005; Geehan et al. 2006; Tempel et al. 2007). The first step in such an analysis was done by Watson et al. (2006) (hereafter denoted by **W06**), who analyzed the diffuse emission from the 5 central arcmin, using the data processed by Shirey et al. (2001). We repeat the analysis of the central part of the M31, processing more observations, and extend the analysis to the off-centre region ( $5' - 13'$ ). We also analyze the uncertainties in the DM distribution in the central part of M31. The outer region of M31 has much fainter diffuse emission than its central part (c.f. e.g. Takahashi et al. 2004, Fig. 8), and uncertainties in the determining of the distribution of DM in this region are lower. All this allows us to strengthen the restrictions on the parameters of sterile neutrino DM, while using more conservative estimates of the DM signal.

The paper is organized as follows. We briefly summarize the properties of decaying DM in Section 2. The description of DM in M31 and expected DM decay flux is computed in Section 3. In Section 4 we describe the methodology of EPIC MOS and PN data reduction which we perform by using two different methods: *Extended Sources Analysis Software* (ESAS) and single background subtraction method (SBS). In Section 5 we fit the spectra and obtain the restrictions on sterile neutrino parameters. Finally, we discuss our results in Section 6.

## 2 DECAYING DARK MATTER MODEL

The flux of the DM decay from a given direction (in photons  $\text{s}^{-1}\text{cm}^{-2}$ ) is given by

$$F_{DM} = \frac{\Gamma E_\gamma}{m_s} \int_{fov\ cone} \frac{\rho_{DM}(\mathbf{r})}{4\pi|\mathbf{D}_L + \mathbf{r}|^2} \mathbf{d}\mathbf{r}. \quad (1)$$

Here  $\mathbf{D}_L$  is the *luminosity* distance between an observer and the centre of an observed object,  $\rho_{DM}(\mathbf{r})$  is the DM density, and the integration is performed over the DM distribution inside the (truncated) cone – solid angle, spanned by the field of view (FoV) of the X-ray satellite. In case of distant objects<sup>4</sup>, Eq. (1) can be simplified:

$$F_{DM} = \frac{M_{DM}^{fov} \Gamma E_\gamma}{4\pi D_L^2 m_s}, \quad (2)$$

where  $M_{DM}^{fov}$  is the mass of DM within a telescope field of view,  $m_s$  – mass of the sterile neutrino DM. In the case of small FoV, Eq. (2) simplifies to

$$F_{DM} = \frac{\Gamma S_{DM} \Omega E_\gamma}{4\pi m_s}, \quad (3)$$

where

$$S_{DM} = \int_{l.o.s.} \rho_{DM}(r) dr \quad (4)$$

is the DM column density (the integral goes along the line of sight),  $\Omega \ll 1$  - FoV solid angle.

The decay rate of the sterile neutrino DM is equal to (Pal & Wolfenstein 1982; Barger et al. 1995)<sup>5</sup>

$$\Gamma = \frac{9\alpha G_F^2}{1024\pi^4} \sin^2(2\theta) m_s^5 \approx 1.38 \cdot 10^{-30} s^{-1} \left[ \frac{\sin^2(2\theta)}{10^{-8}} \right] \left[ \frac{m_s}{1 \text{ keV}} \right]^5. \quad (5)$$

Here  $m_s$  is the sterile neutrino mass,  $\theta$  - mixing angle between sterile and active neutrinos. From a compact cloud of sterile neutrino DM we therefore obtain the flux:

$$F_{DM} \approx 6.38 \cdot 10^6 \frac{\text{keV}}{\text{cm}^2 \cdot \text{s}} \left[ \frac{M_{DM}^{fov}}{10^{10} M_\odot} \right] \left[ \frac{\text{kpc}}{D_L} \right]^2 \sin^2(2\theta) \left[ \frac{m_s}{1 \text{ keV}} \right]^5. \quad (6)$$

## 3 ANDROMEDA GALAXY (M31)

M31, or Andromeda galaxy, is one of the nearest galaxies, excluding dwarves; it is located at the distance  $D_L = 784 \pm 13 \pm 17$  kpc (Stanek & Garnavich 1998). Its proximity allows us to resolve most of its point sources and extract the spectrum of diffuse emission of its central part.

Available *XMM-Newton* (Jansen et al. 2001) observations cover the region of central  $15'$  of M31 with exposure time greater than 100 ksec (see Table 1). W06 used the *XMM-Newton* data on central  $5'$  of M31 (observation 0112570401 processed by Shirey et al. (2001), exposure time about 30 ksec) to produce restrictions on the parameters of sterile neutrino DM. The sufficient increase of photon statistics enables us to analyze the outer ( $5' - 13'$ ) faint part of M31, which, however, has a significant mass of DM (see Section 3.1 below).

In this work we will analyze two different spatial regions of Andromeda galaxy: region `circle5`, which corresponds to  $5'$  circle around the centre of M31, and region `ring5-13`, which corresponds to the ring with inner and outer radii of  $5'$  and  $13'$ , respectively.

### 3.1 Calculation of DM mass

To obtain the restriction on parameters of the decaying DM, we should calculate the total DM mass  $M_{DM}^{fov}$ , which corresponds to both spatial regions: `circle5` and `ring5-13`, both with and without resolved point sources. To estimate the systematic uncertainties of the evaluation of the DM decay signal and to find the most conservative estimate for it, we analyze various available DM profiles (Kerins et al. 2001; Klypin et al. 2002; Widrow & Dubinski 2005; Geehan et al. 2006; Carignan et al. 2006; Tempel et al. 2007):

<sup>4</sup> Namely, if luminosity distance  $D_L$  is much greater than the characteristic scale of the DM distribution.

<sup>5</sup> Our decay rate is 2 times smaller than the one used in W06. This is due to the Majorana nature of the sterile neutrino, which we consider (c.f. Barger et al. 1995). The final constraints for a Dirac particle would thus be 2 times stronger.

Obs. ID	Starting time, UTC	Filter	Cleaned MOS1/MOS2/PN exposure, ks
0112570401	2000-06-25 08:12:41	Medium	30.8/31.0/27.6
0109270101	2001-06-29 06:15:17	Medium	40.1/41.9/47.4
0112570101	2002-01-06 18:00:56	Thin	63.0/63.0/55.3

**Table 1.** Observations of the central part of M31, used in our analysis.

Model	circle5	ring5-13	13 arcmin sphere, MC result	13 arcmin sphere, analytical result
K1, with sources	3.27 ± 0.01	12.49 ± 0.03	5.84 ± 0.02	5.84
K2, with sources	11.88 ± 0.03	23.75 ± 0.09	20.76 ± 0.09	-
GFBG, with sources	6.59 ± 0.02	20.46 ± 0.06	13.40 ± 0.03	13.39
KING, with sources	6.68 ± 0.01	24.61 ± 0.05	14.80 ± 0.02	14.80
MOORE, with sources	7.34 ± 0.02	19.48 ± 0.02	13.79 ± 0.02	13.78
N04, with sources	7.68 ± 0.03	22.89 ± 0.07	15.16 ± 0.06	15.18
NFW, with sources	11.08 ± 0.04	40.5 ± 0.1	22.3 ± 0.1	22.25
BURK, with sources	6.71 ± 0.02	27.97 ± 0.03	15.90 ± 0.05	15.90
KER, with sources	5.35 ± 0.02	22.45 ± 0.04	11.56 ± 0.03	11.56
M31A, with sources	5.95 ± 0.01	16.45 ± 0.02	11.03 ± 0.02	-
M31B, with sources	4.99 ± 0.01	14.24 ± 0.01	9.40 ± 0.02	-
M31C, with sources	5.60 ± 0.01	16.12 ± 0.01	10.29 ± 0.02	-

**Table 2.** DM mass (in  $10^9 M_\odot$ ) inside regions, used in our analysis: results of our Monte Carlo integration. The point sources are not excluded here. The 95% statistical errors are also shown. The DM distributions of Klypin et al. (2002) (before and after adiabatic contraction), Geehan et al. (2006) and Kerins et al. (2001) are marked as “K1”, “K2”, “GFBG” and “KER”, respectively. The DM distributions from Tempel et al. (2007) are marked as “KING”, “MOORE”, “N04”, “NFW” and “BURK” (see text). The DM distributions from Widrow & Dubinski (2005) are marked as “M31A”, “M31B” and “M31C”.

- **(K1)** *Before*<sup>6</sup> adiabatic contraction stage, Klypin et al. (2002) assume that DM distribution is purely Navarro-Frenk-White (NFW) (Navarro et al. 1997):

$$\rho_{DM}(r) = \frac{1}{4\pi [\log(1+C) - C/(1+C)]} \frac{M_{vir}}{r(r+r_s)^2}. \quad (7)$$

The parameters of this NFW distribution (in terms of the favored C1 model of Klypin et al. 2002) are:  $M_{vir} = 1.60 \times 10^{12} M_\odot$ ;  $r_s = 25.0$  kpc;  $C = 12$ .

- **(K2)** This non-analytical model is the result of adiabatic contraction of the **K1** profile, described above. To obtain it, we extract the data from the Fig. 4 of Klypin et al. (2002). In the top part of this figure the dot-dashed curve is the contribution of the DM halo to the total M31 mass distribution (C1 model of Klypin et al. 2002). As the precise form of this mass distribution is not analytic, we scanned this curve and produced the file with numerical values of enclosed mass  $M_{DM}(r)$  within the *sphere* of radius  $r$ . After that, we interpolated the  $M_{DM}(r)$ , and evaluated the radial density distribution

$$\rho_{DM}(r) = \frac{1}{4\pi r^2} \frac{dM_{DM}(r)}{dr}. \quad (8)$$

- **(GFBG)** Preferred Navarro-Frenk-White distribution from Geehan et al. (2006):  $M_{vir} = 6.80 \times 10^{11} M_\odot$ ;  $r_s = 8.18$  kpc;  $C = 22$ .
- **(KER)** Isothermal profile used in Kerins et al. (2001):

$$\rho_{KER}(r) = \begin{cases} \rho_h(0) \frac{a^2}{a^2+r^2} & r \leq R_{max}, \\ 0 & r > R_{max}. \end{cases} \quad (9)$$

where  $\rho_h(0) = 0.23 M_\odot \text{pc}^{-3}$ ,  $a = 2$  kpc,  $R_{max} = 200$  kpc.

- **(M31A-C)** Profiles of Widrow & Dubinski (2005). In this paper the authors propose several models, which differ by the relative disk/halo contribution. These non-analytical models (M31a-d) incorporate an exponential disk, a Hernquist model bulge, an NFW

halo (before contraction) and a central supermassive black hole. The stability against the formation of bars was numerically studied.<sup>7</sup>

We also use density distributions from the recent paper of Tempel et al. (2007). The main aim of this paper is to derive the DM density distribution in the central part of M31 (0.02-35 kpc from the centre).

- **(KING)** Modified isothermal profile (King 1962; Einasto et al. 1974):

$$\rho_{ISO}(r) = \begin{cases} \rho_0 \left( \left[ 1 + \frac{r^2}{r_c^2} \right]^{-1} - \left[ 1 + \frac{r_0^2}{r_c^2} \right]^{-1} \right) & r \leq r_0, \\ 0 & r > r_0. \end{cases} \quad (10)$$

where  $\rho_0 = 0.413 M_\odot \text{pc}^{-3}$ ,  $r_c = 1.47$  kpc,  $r_0 = 117$  kpc.

- **(MOORE)** Moore profile (Moore et al. 1999):

$$\rho_{MOORE}(r) = \frac{\rho_c}{\left(\frac{r}{r_c}\right)^{1.5} \left[ 1 + \left(\frac{r}{r_c}\right)^{1.5} \right]}, \quad (11)$$

where  $\rho_c = 4.43 \cdot 10^{-3} M_\odot \text{pc}^{-3}$ ,  $r_c = 17.9$  kpc.

- **(N04)** Density distribution of Navarro et al. (2004):

$$\rho_{N04}(r) = \rho_c \exp \left[ -\frac{2}{\alpha} \left( \frac{r^\alpha}{r_c^\alpha} - 1 \right) \right], \quad (12)$$

where parameter  $\alpha$ , according to simulations, equals to 0.172 ± 0.032 (Navarro et al. 2004). For **N04** we take  $\alpha = 0.17$ ,  $\rho_c = 6.42 \cdot 10^{-3} M_\odot \text{pc}^{-3}$ ,  $r_c = 11.6$  kpc.

- **(NFW)** Navarro-Frenk-White profile:

$$\rho_{NFW}(r) = \frac{\rho_c}{\frac{r}{r_c} \left[ 1 + \left(\frac{r}{r_c}\right)^2 \right]}, \quad (13)$$

<sup>6</sup> In contrast to the other models, this model does not describe the current DM distribution, but helps our understanding the time evolution of DM mass inside constant FoV.

<sup>7</sup> We do not use the fourth model (M31d), because in Widrow & Dubinski (2005) it was found that this model develops a bar, which rules it out experimentally.

Model	circle5	Removed from circle5, %	ring5-13	Removed from ring5-13, %
K1, without sources	$0.767 \pm 0.004$	76.6	$9.71 \pm 0.02$	22.3
K2, without sources	$2.31 \pm 0.02$	80.4	$18.09 \pm 0.08$	23.9
GFBG, without sources	$1.48 \pm 0.01$	77.4	$15.77 \pm 0.06$	23.0
KING, without sources	$1.64 \pm 0.01$	75.5	$18.99 \pm 0.06$	22.9
MOORE, without sources	$1.52 \pm 0.01$	79.2	$14.98 \pm 0.03$	23.1
N04, without sources	$1.70 \pm 0.02$	77.7	$17.62 \pm 0.05$	23.0
NFW, without sources	$2.59 \pm 0.01$	76.7	$31.34 \pm 0.07$	22.5
BURK, without sources	$1.67 \pm 0.02$	75.1	$21.68 \pm 0.02$	22.5
KER, without sources	$1.33 \pm 0.01$	75.0	$17.42 \pm 0.04$	22.5
M31A, without sources	$1.24 \pm 0.01$	79.3	$12.66 \pm 0.02$	22.9
M31B, without sources	$1.04 \pm 0.01$	79.1	$10.98 \pm 0.01$	23.0
M31C, without sources	$1.21 \pm 0.01$	78.4	$12.43 \pm 0.01$	22.9

**Table 3.** DM mass (in  $10^9 M_\odot$ ) without point sources: results of our Monte Carlo integration. The fraction of DM, removed together with the point sources, is also shown. All notations are the same as in previous table.

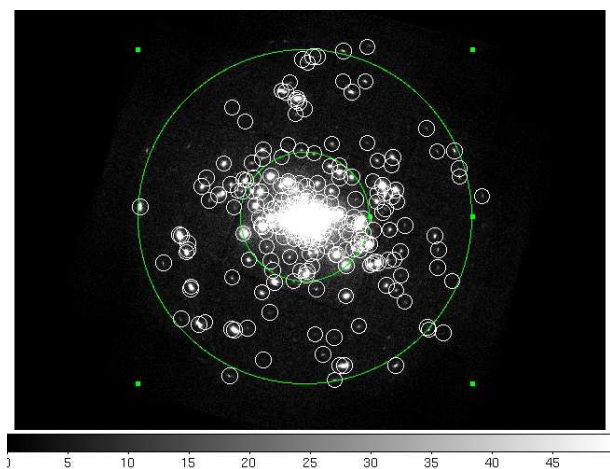


**Figure 1.** Selected regions in the central part of M31 (shown in linear scale). Small circles correspond to excluded point source regions, large circles have radius of 5 and 13 arcmin.

where  $\rho_c = 5.20 \cdot 10^{-2} M_\odot \text{pc}^{-3}$ ,  $r_c = 8.31 \text{ kpc}$ .

- **(BURK)** Burkert profile (Burkert 1995):

$$\rho_{BURK}(r) = \frac{\rho_0}{\left(1 + \frac{r}{r_c}\right) \left(1 + \frac{r^2}{r_c^2}\right)}, \quad (14)$$

where  $\rho_0 = 0.335 M_\odot \text{pc}^{-3}$ ,  $r_c = 3.43 \text{ kpc}$ .

The computed DM masses within the FoV for all these profiles are shown in Table 2. We see that for the model used by W06 (model **K2** in our notations), our estimate of the DM mass within the central  $5'$  coincides with the value used in W06:  $M_5 = (1.3 \pm 0.2) \cdot 10^{10} M_\odot$ . Notice, however, that to obtain the diffuse spectrum, we extracted all point sources, resolved with the significance  $\geq 4\sigma$ . Each source was removed with the circle of the radius of  $36''$  (see Sec. 4.1 for details). This led to the reduction of the area of the FoV by about 70% in case of **circle5** region (c.f. Fig. 1). As the density of the DM changes with the off-centre distance and this change can be significant (c.f. Fig. 2), we performed the integration of the DM density distribution over the FoV with excluded point sources. To calculate the DM mass in such “swiss cheese” regions (Fig. 1), we used Monte Carlo integration. The results are summarized in the Table 3.

To check possible systematic effects of our Monte Carlo integration method, we also obtained the values of enclosed mass

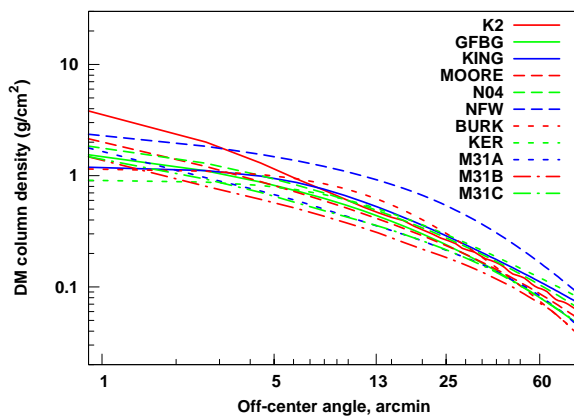


**Figure 2.** M31 DM column density versus off-centre angle as result of our Monte Carlo integration, based on DM profiles of Sec. 3.1. (Point sources are not excluded).

inside the 13 arcmin *sphere*, and compared them with analytical calculations (wherever possible). Such an error does not exceed the purely statistical error of numerical integration (see Table 2).

As one can see from Tables 2-3, the most conservative DM model, describing regions **circle5** and **ring5-13**, is the model **M31B** of Widrow & Dubinski (2005). Therefore, to obtain restrictions on the DM parameters in what follows, we will use the DM mass estimates based on this model.

For the DM distributions listed above, we also build the DM column density  $S_{DM}$  (given by Eq. (4)) versus off-centre angle. The result is shown on Fig. 2. It is clearly seen that, in the off-centre regions, there is still a lot of DM, and, together with the fact that the surface brightness of X-ray diffuse emission falls rapidly outside the central  $5'$  (c.f. Takahashi et al. 2004), improving the restrictions of W06 by analyzing the off-centre  $5'$ – $13'$  ring. Moreover, as one can see from Table 3 and Fig. 2, the uncertainty of DM in this region is less than in the **circle5** region.

To estimate the additional contribution from the Milky Way DM halo in the direction of M31, we use an isothermal DM distribution (as e.g. in Boyarsky et al. 2006d, 2007). The DM column density is equal to

$$S_{MW,DM} = \frac{v_h^2}{8\pi r_c G_N} K(\phi), \quad (15)$$

where  $v_h = 170 \text{ km s}^{-1}$ ,  $r_c = 4 \text{ kpc}$  – parameters of isothermal model,  $r_\odot = 8 \text{ kpc}$  – distance from Earth to the Galactic Centre, and

$$K(\phi) = \frac{r_c}{R(\phi)} \begin{cases} \frac{\pi}{2} + \arctan\left[\frac{r_\odot \cos \phi}{R(\phi)}\right], & \cos \phi \geq 0 \\ \arctan\left[\frac{R(\phi)}{r_\odot \cos \phi}\right], & \cos \phi < 0. \end{cases} \quad (16)$$

Here  $\phi$  is defined via  $\cos \phi = \cos l \cos b$  for an object with galactic coordinates  $(b, l)$ ,  $R(\phi) = (r_c^2 + r_\odot^2 \sin^2 \phi)^{1/2}$ . For Andromeda galaxy ( $l = 121.17^\circ$ ,  $b = -21.57^\circ$ , i.e.  $\phi = 118.77^\circ$ ) one obtains

$$S_{MW,DM} \approx 6.2 \cdot 10^{-3} g \cdot \text{cm}^{-2} = 3.5 \times 10^{27} \text{ keV} \cdot \text{cm}^{-2} \quad (17)$$

According to Fig. 2, the MW contributes  $< 5\%$  to the total DM column density along the central part of Andromeda galaxy, and therefore will be neglected in what follows.

#### 4 DATA REDUCTION AND BACKGROUND SUBTRACTION

To obtain restrictions on the parameters of the sterile neutrino, we need to analyze diffuse emission from faint extended regions of M31. There exist several well-developed background subtraction procedures for the diffuse sources (see, for instance, *XMM-Newton* SAS User Guide<sup>8</sup>, Nevalainen et al. 2005, Read & Ponman 2003). In this paper we use two methods of background subtraction:

##### 4.1 Extended Sources Analysis Software (ESAS)

This method, recently developed by ESAC/GSFC team<sup>9</sup>, allows one to subtract instrumental and cosmic backgrounds separately. It seems to be better than the subtraction of the scaled blank-sky background, averaged through the entire *XMM-Newton* Field of View (see next subsection for details), as instrumental and cosmic backgrounds (due to their different origin) have different vignetting correction factors. ESAS models instrumental background from “first principles”, using filter-wheel closed data and data from the unexposed corners of archived observations. Using this software, we are assured that no DM line can be in our background, in contrast with the “black sky” background subtraction method and, especially, local background subtraction (used e.g. in Shirey et al. (2001) to produce the diffuse spectrum of central  $5'$  of M31). The price to pay is the necessity of modelling cosmic background.

To prepare the EPIC MOS (Turner et al. 2001) event lists, we used the ESAS script `mos-filter`. After running `mos-filter`, we produced cleaned MOS images in sky coordinates, which were used to obtain the mosaic image (with the help of SAS v7.0.0 tool `emosaic`). We used these event lists and images to find the point sources using SAS task `edetect_chain`. Source detections were accepted with likelihood values above 10 (about  $4\sigma$ ). We found 243 point sources in this way. After that, we excluded each of them within the circular region of the radius  $36''$ , which corresponds to the removal of  $\sim 70 - 85\%$  of total encircled energy, depending on the on-axis angle (see *XMM users handbook*<sup>10</sup> for details). The constructed mosaic image with detected point sources and selected regions is shown in Fig. 1.

We obtained the MOS1 and MOS2 spectra and constructed

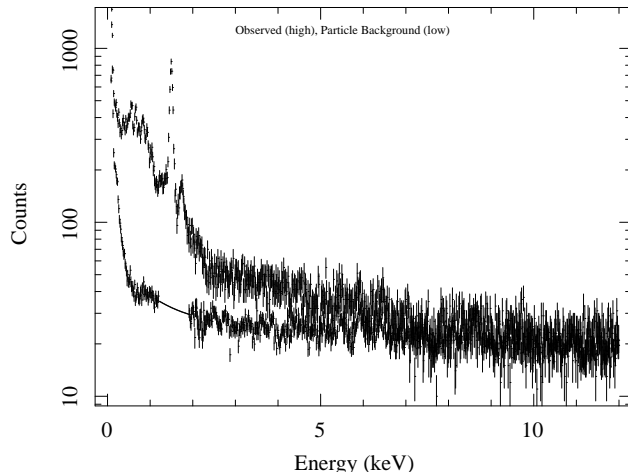


**Figure 3.** Observed spectrum (top) and modelled instrumental background (bottom) MOS1 from ObsID 0112570101, region ring5-13. It can be seen that the spectrum and modelled background almost coincide for  $E > 7 \text{ keV}$ .

the corresponding background with the help of ESAS scripts `mos-spectra`<sup>11</sup> and `xmm-back`, respectively.

Finally, we grouped the spectra with corresponding response and background files with the help of FTOOL `grppha`, a part of HEASOFT v6.1. To ensure Gaussian statistics, the minimum number of counts per bin was set to be 50.

The ESAS method of background subtraction, however, has several difficulties. The number of fitting parameters substantially increases, hence it is harder to find true minimum of  $\chi^2$ . The quantitative analysis of the 1.3–1.8 keV energy range is also not possible, because of the presence of two strong unmodelled instrumental lines (see Figs. 3, 4). EPIC-PN (Strüder et al. 2001) data reduction is not yet implemented in ESAS. Therefore, to cross-check the results obtained with the help of ESAS software, we also processed EPIC data with the help of the blank-sky data subtraction (SBS) method (Read & Ponman 2003).

##### 4.2 Blank-sky background subtraction (SBS)

We processed the same M31 observations (Table 1) as in the previous Section, using both MOS and PN data. To subtract the blank-sky background we firstly cast it at the position of M31 with the help of the script `skycast`<sup>12</sup>, written by the *XMM-Newton* group in Birmingham. The scaling coefficient was derived by comparing count rates for  $E \geq 10 \text{ keV}$  from source regions and background sample. To produce spectra, ARF, RMF and to group them correctly (we needed to extract them from non-circular regions), we modified the Birmingham script `createspectra`<sup>13</sup>. The spatial regions were chosen similarly to those in Sec. 4.1, so it would be possible to compare the results of the two different methods (see Sec.5.3).

When analyzing PN data, we found that the role of out-of-time (OOT) events was significant. This is due to the fact that the rate of OOT events is proportional to the total rate inside the

<sup>8</sup> [http://xmm.esac.esa.int/external/xmm\\_user\\_support/documentation/ssa\\_snrfgg/USC](http://xmm.esac.esa.int/external/xmm_user_support/documentation/ssa_snrfgg/USC)

<sup>9</sup> We use ESAS version 1.0.

<sup>10</sup> [http://xmm.esac.esa.int/external/xmm\\_user\\_support/documentation/](http://xmm.esac.esa.int/external/xmm_user_support/documentation/)

<sup>11</sup> To produce correct RMF file, we changed in the script `mos-spectra` `maptype=psf` to `rmfgen detmaptype=dataset`.

<sup>12</sup> <http://www.sr.bham.ac.uk/xmm3/skycast>

<sup>13</sup> <http://www.sr.bham.ac.uk/xmm3/createspectra>

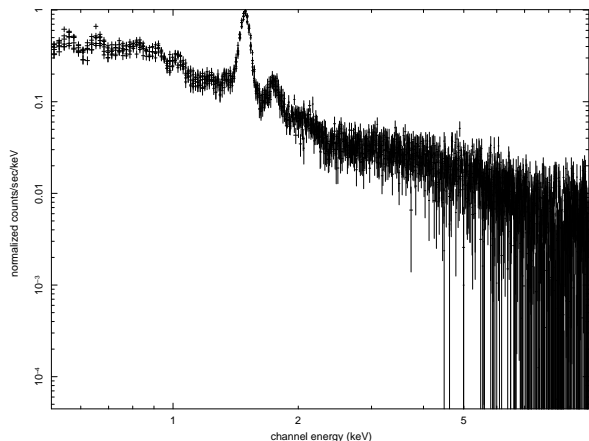


**Figure 4.** Folded spectra from ring5-13 region (by ESAS method), with excluded point sources. The presence of two unsubtracted instrumental lines at 1.49 keV and 1.75 keV is clearly shown.

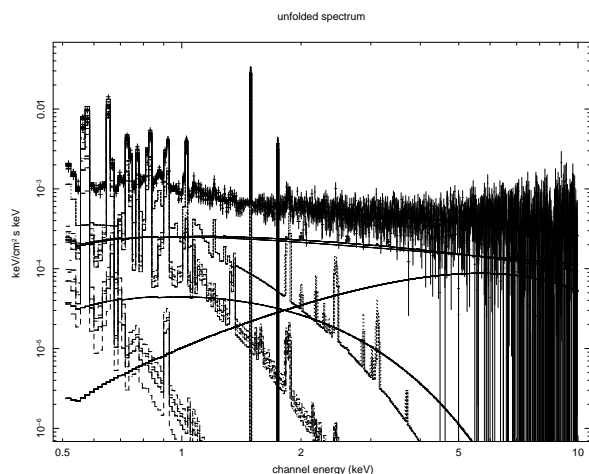


**Figure 5.** Unfolded spectra and best-fit model from ring5-13 region (by ESAS method), with excluded point sources. The “line forest” at energies lower 2.0 keV is clearly visible.

full PN FoV rather than the rate of diffuse emission (outside excluded point sources). Therefore, it was necessary to remove the OOT events from the PN event lists. Most of the OOT events (from the bright point sources) form strips in the images and can be easily removed with the help of spatial filtering. This additional filtering also slightly reduced the possible DM signal, which was (in this outer region) nearly proportional to BACKSCALE keyword. This was accounted for when producing SBS PN restrictions.

## 5 FITTING THE SPECTRA IN XSPEC AND PRODUCING RESTRICTIONS

After we have prepared the data (with ESAS and SBS background subtraction methods) we fitted obtained spectra with realistic model (using Xspec spectral fitting package version 11.3.2, Arnaud 1996). The results of our fits are shown in Tables 4, 5, 6. Notice that the fit results obtained by two background subtraction methods (ESAS and SBS) coincide within the 90% confidence in-

terval (Table 4).<sup>14</sup> Also shown in Table 4 are the results of Takahashi et al. (2004), who analyzed diffuse emission in the central 6′ of M31.<sup>15</sup> Below we discuss separately the fitting of ESAS and SBS spectra.

### 5.1 ESAS spectra

We build 0.5 – 10.0 keV MOS spectra of circle5 and ring5-13 regions for 3 observations from Table 1.<sup>16</sup> Thus for each spatial region we have 6 spectra to fit - from observations with MOS1 and MOS2 cameras. We fix the model parameters to be equal for all six spectra from the same spatial region (except for normalization of the remaining soft proton background, as the spectra from different observations are slightly different).

Since ESAS software subtracts only the instrumental background component, the remaining cosmic background should be modelled. The cosmic background component is modelled with the help of Xspec model `apec+(apec+pow)*wabs`, according to the ESAS manual. A cool ( $\sim 0.1$  keV), unabsorbed apec (Smith et al. 2001) component represents the thermal emission from the Local Hot Bubble. The hot ( $\sim 0.25$  keV), absorbed apec component represents emission from the hotter halo and/or intergalactic medium. The last, absorbed powerlaw component with powerlaw index  $\Gamma = 1.41$  represents the unresolved background from cosmological sources. We kept its normalization fixed for each region; it corresponds to  $8.88 \cdot 10^{-7}$  Xspec units per square arcmin, or to 10.5 photons  $\text{keV}^{-1} \text{s}^{-1} \text{cm}^{-2} \text{sr}^{-1}$ . The corresponding hydrogen column density in wabs was left to vary below its Galactic value  $n_H = 6.7 \cdot 10^{20} \text{cm}^{-2}$  (Morrison & McCammon 1983). To model the soft proton contamination, we used `bknppow/b` model (we fix its break energy at 3.3 keV), where index /b means that this component is not folded through the instrumental effective area (in Xspec versions 11 and earlier).

The `diskbb+bbbody` (the same as the LMXB model in Takahashi et al. 2004) component describes the point sources, which were not excluded. We fitted the diffuse M31 component in outer regions with the help of the sum of three `vmekal` (Mewe et al. 1986; Liedahl et al. 1995) models with fixed temperatures and abundances. The wabs column density was fixed at its Galactic value.

### 5.2 SBS spectra

We fitted the data from MOS and PN cameras, processed using SBS method (both separately and combined). As both cosmic and instrumental background is subtracted in SBS method, we fitted MOS and PN spectra on `wabs*(diskbb+bbbody+vmekal+vmekal+vmekal)` Xspec model at the energy range 0.6–10.0 keV (0.6–12.0 keV in case of PN camera). The reduced  $\chi^2$  obtained by fitting our spectra are shown in Table 5; fit parameters are shown in Table 4.

<sup>14</sup> The value of  $\text{norm}_{bb}$  also coincides within 90% confidence interval if one propagates the uncertainty of blank-sky background normalization.

<sup>15</sup> The appreciable difference between our errors and those of Takahashi et al. (2004) is due to the fact that we did not fix the metal abundances equal to each other. This was essential for our purposes, because of the clear presence of the “line forest” at energies below 2.0 keV (see Sec. 5.3 and Fig. 5).

<sup>16</sup> We exclude the region 1.3–1.8 keV due to the presence of two strong unmodelled instrumental lines, see Sec. 4.1.

Parameters	$kT_{disk}$ , keV	$norm_{disk}$	$norm_{hb}$ , $10^{-6}$	$kT_1$ , keV	$norm_1$ , $10^{-3}$	$kT_2$ , keV	$norm_2$ , $10^{-3}$	$kT_3$ , keV	$norm_3$ , $10^{-3}$
circle5,ESAS	$0.722^{+0.236}_{-0.103}$	$0.098^{+0.098}_{-0.060}$	$6.71^{+1.07}_{-1.07}$	$0.634^{+0.169}_{-0.059}$	$0.16^{+11.55}_{-0.04}$	$0.396^{+0.113}_{-0.141}$	$0.69^{+0.75}_{-0.31}$	$0.171^{+0.031}_{-0.054}$	$1.08^{+63.44}_{-0.45}$
circle5,SBS	$0.549^{+0.171}_{-0.030}$	$0.117^{+0.116}_{-0.047}$	$8.61^{+0.92}_{-0.65}$	$0.640^{+0.144}_{-0.184}$	$0.26^{+1.09}_{-0.26}$	$0.385^{+0.069}_{-0.107}$	$0.60^{+0.64}_{-0.122}$	$0.146^{+0.104}_{-0.122}$	$0.35^{+2.65}_{-0.35}$
ring5-13,ESAS	$0.655^{+0.192}_{-0.037}$	$0.249^{+0.386}_{-0.162}$	$43.0^{+4.5}_{-9.3}$	$0.615^{+0.121}_{-0.138}$	$0.53^{+0.50}_{-0.53}$	$0.352^{+0.092}_{-0.118}$	$0.36^{+0.63}_{-0.36}$	$0.102^{+0.199}_{-0.033}$	$10.1^{+38.6}_{-7.7}$
ring5-13,SBS	$0.628^{+0.229}_{-0.139}$	$0.126^{+0.266}_{-0.092}$	$25.6^{+4.0}_{-3.2}$	$0.594^{+0.160}_{-0.082}$	$1.25^{+34.19}_{-0.69}$	$0.375^{+0.040}_{-0.087}$	$2.48^{+38.4}_{-1.93}$	$0.155^{+0.043}_{-0.074}$	$10.4^{+55.9}_{-10.4}$
TOKM, EPIC	$0.88^{+0.08}_{-0.07}$			$0.61^{+0.03}_{-0.02}$		$0.30^{+0.03}_{-0.02}$		$0.12^{+0.03}_{-0.02}$	
TOKM, ACIS	$0.89^{+0.02}_{-0.01}$			$0.60^{+0.03}_{-0.02}$		$0.30^{+0.01}_{-0.01}$		$0.10^{+0.01}_{-0.01}$	

**Table 4.** Model parameters from regions `circle5` and `ring5-13`. Also shown are 90% confidence intervals for fitted parameters. Results of Takahashi et al. (2004) (6′ circular region in this case) are marked as “TOKM”.

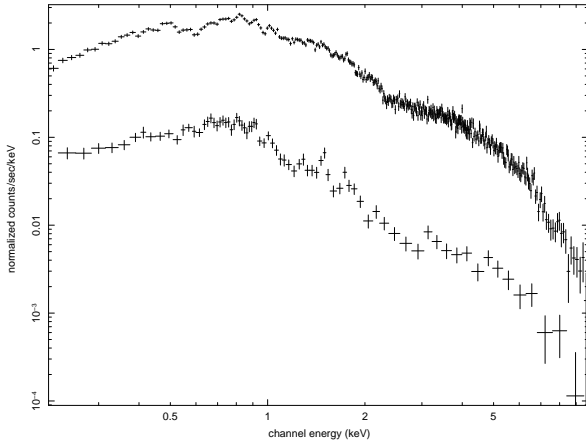


**Figure 6.** Folded MOS1 spectra from `circle5` region, ObsID 0112570401, with (top) and without (bottom) point sources.

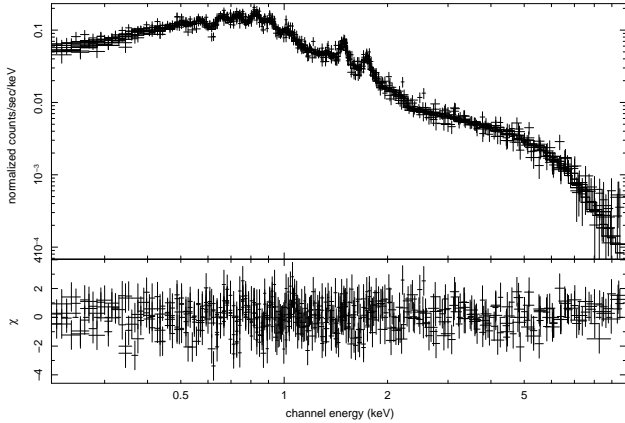


**Figure 7.** Folded spectra and best-fit model from `circle5` region, with excluded point sources.

Region	Reduced $\chi^2$	Number d.o.f.
ESAS, <code>circle5</code>	1.071	399
SBS MOS, <code>circle5</code>	1.102	371
ESAS, <code>ring5-13</code>	1.109	1608
SBS MOS, <code>ring5-13</code>	0.994	1735
SBS PN, <code>ring5-13</code>	1.007	2754
SBS PN-OOT, <code>ring5-13</code>	0.995	2715
SBS MOSPN-OOT, <code>ring5-13</code>	1.009	4082

**Table 5.** Reduced  $\chi^2$  for our regions.

### 5.3 Producing restrictions on sterile neutrino parameters

In this subsection we describe two different techniques of searching for the narrow (compared to the spectral resolution of *XMM-Newton*) decay line in the spectra, processed by ESAS and SBS methods.

As shown on Fig. 5, above 2.0 keV there are few emission lines in the model of the spectrum of M31, and continuum emission dominates. In this case, it is possible to apply the “statistical” method, discussed e.g. in Boyarsky et al. (2006d). Namely, after fitting the spectra with the selected models (Secs. 5.1–5.2 above), we add an extra Gaussian line with the help of Xspec command `addcomp`. We then freeze its energy  $E_\gamma$ , leave the line width  $\sigma$  to vary within 0–10 eV, and repeat the fit. For each line energy, we re-fit the model and derive an upper limit on the flux in the Gaussian line, allowing all other model parameters to vary. In particular we allow the abundances of heavy elements, that produce the thermal emission lines to vary. This produces the most conservative restrictions as the added line could account for some of the flux from the thermal components. After that we calculate the  $3\sigma$  error with the help of Xspec command `error (line norm) 9.0`. To obtain conservative upper limits, we allow as much freedom as possible for the parameters of the thermal model. The  $3\sigma$  upper limit on the DM line flux is shown in Fig. 8. These flux restrictions can be turned into constraints on parameters of the sterile neutrino ( $m_s$  and  $\sin^2(2\theta)$ ), using Eq. (6) and the value of the  $M_{DM}^{fov}$  from the Table 3 for the model **M31B**.

Below 2.0 keV, there are a lot of strong emission lines, which dominate over the continuum, creating a “line forest”. As the intrinsic widths of these lines are much more narrow than the spectral resolution of EPIC cameras of *XMM-Newton*, and the abundances of various elements are known with large uncertainties, it is very hard to reliably distinguish these emission lines from a possible DM decay line. Therefore, to produce robust constraints, we apply the “full flux” method below 2 keV. In this method, we equate the DM line flux to the full flux plus 3 flux uncertainties over the energy interval  $\Delta E$  equal to the spectral resolution of the instrument.<sup>17</sup>

We also produce *model-dependent* “statistical” constraints below 2.0 keV. To reduce model uncertainty, we fix most metal abundances at their values known from optical observations of M31 (Jacoby & Ciardullo 1999; Jacoby & Ford 1986; Dennefeld & Kunth 1981; Blair et al. 1982). The confidence ranges of these abundances are shown in Table 6.

To compare our results with previous work on M31 (Watson et al. 2006, hereafter W06) we performed full flux analysis in the

<sup>17</sup> To find the proper value of  $\Delta E$ , we fold thin Gaussian line with appropriate RMF, and then evaluate FWHM of obtained broadened line. The FWHM  $\Delta E$ , calculated in such a manner, slowly increases with line energy and changes from 0.18 keV to 0.21 keV in the 0.5–2.0 keV energy region.

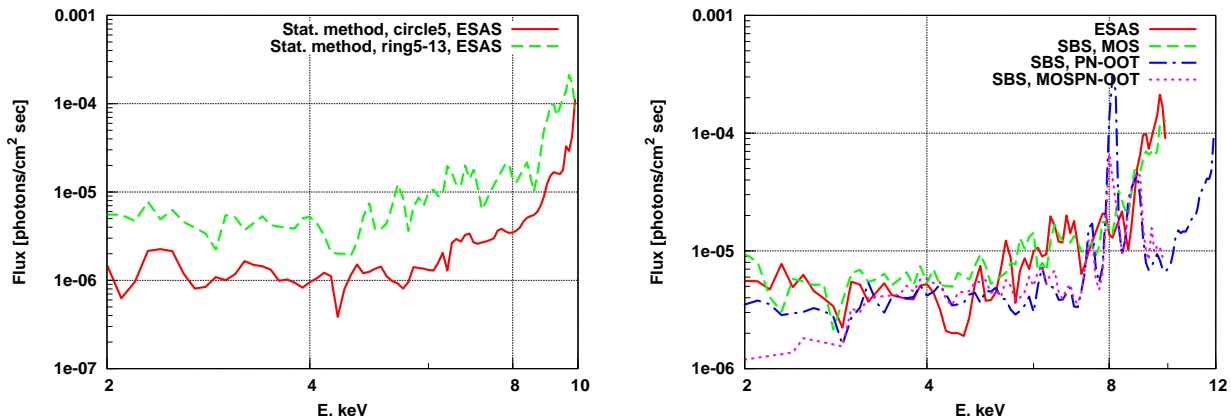


**Figure 8.**  $3\sigma$  upper limit on the DM line flux (the region of parameter space *above* the curves is excluded). *Left panel:* upper limits from the different spatial regions for the spectra, processed by ESAS method. *Right panel:* upper limits for the ring5–13 region for both ESAS and SBS methods.

	He	C	N	O	Ne	S	Ar
Jacoby & Ciardullo (1999)	$1.3^{+0.3}_{-0.3}$	$1.0^{+0.7}_{-0.4}$	$1.1^{+1.0}_{-0.6}$	$0.3^{+0.2}_{-0.1}$	$0.3^{+0.2}_{-0.1}$	$1.5^{+1.2}_{-0.7}$	$0.3^{+0.2}_{-0.1}$
Jacoby & Ford (1986)	$1.3^{+0.4}_{-0.3}$	-	$0.5^{+0.3}_{-0.2}$	$0.4^{+0.1}_{-0.1}$	$0.5^{+0.2}_{-0.2}$	-	-
Dennefeld & Kunth (1981)	-	0.2	$1.0^{+0.2}_{-0.2}$	$0.3^{+0.1}_{-0.1}$	-	$0.8^{+0.5}_{-0.5}$	-
Blair et al. (1982), SNRs	$1.6^{+0.3}_{-0.3}$	-	$0.6^{+0.3}_{-0.3}$	$0.4^{+0.1}_{-0.1}$	$0.9^{+0.1}_{-0.1}$	$0.4^{+0.1}_{-0.1}$	-
Blair et al. (1982), HII regions	-	-	$0.4^{+0.3}_{-0.3}$	$0.9^{+0.5}_{-0.5}$	-	$0.8^{+0.5}_{-0.5}$	-
Our allowed range	1.0..1.9	0.2..1.7	0.1..2.1	0.2..1.4	0.2..1.0	0.3..2.7	0.2..0.5

**Table 6.** Abundances from optical observations (in solar units). Our allowed range of abundances, used for construction the model-dependent restriction (see Sec. 5.3), is also shown.

whole region of energies of the MOS camera of *XMM-Newton*. The results are shown in Fig. 9. One can see that our full flux results from *circle5* region are somewhat weaker than the corresponding results of W06 (by a factor 2–3 in the region  $m_s \sim 4$  keV; more than an order of magnitude at  $m_s \lesssim 2$  keV and  $m_s \gtrsim 12$  keV). There are several reasons for this. As discussed in Sec. 3.1 we use an  $\sim 8$  times lower estimate for the DM mass within the FoV, because we use the more recent and more conservative DM profile of Widrow & Dubinski (2005) and compute the amount of DM by explicit integration over the FoV with removed point sources. At the same time, comparing our diffuse spectrum (Figs. 6–7) with Fig. 1 in W06, we see that the intensity of our diffuse spectrum is  $\sim 2 - 3$  times lower (due to the  $\sim 4$  times larger number of point sources removed). Therefore, one would expect a factor 2–3 difference between our results (as indeed is seen at  $m_s \sim 4$  keV).

An additional discrepancy at low energies is due to the different choice of the energy bin intervals. In W06 the energy bin interval was chosen according to the empirical formula  $\Delta E = E_\gamma/30 = m_s/60$ , while we have determined it using the *XMM-Newton* response matrices (as described in footnote 17 above). The difference is most prominent at low energies: e.g. at  $E \sim 1$  keV we obtain  $\Delta E \approx 0.2$  keV, which is  $\sim 6$  times bigger than the value, used by W06. Therefore, at small energies we would expect constraints about an order of magnitude lower than those of W06, as Fig. 9 indeed demonstrates.

The other important effect, seen in Fig. 9, is the high-energy behaviour. Our restrictions remain nearly constant for  $m_s \gtrsim 12$  keV ( $E_\gamma \gtrsim 6$  keV), in contrast to the steeply decreasing results of W06. This is due to the fact that W06 used an energy-averaged count-rate-to-flux conversion factor (i.e., the telescope effective area): see Sec. IV of W06. However, the effective area of the *XMM-Newton* MOS cameras declines sharply with energy, essentially going to

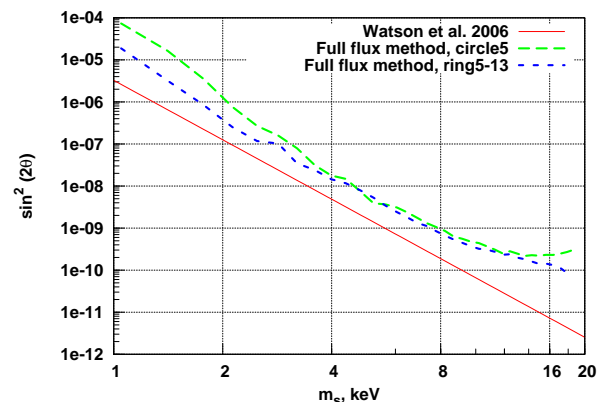


**Figure 9.** Our limits on  $(m_s, \sin^2(2\theta))$  parameters, obtained by using the full flux method from different spatial regions of M31 (a region of parameter space *above* a curve is excluded). The restriction from W06 is shown for comparison.

zero at 9–10 keV.<sup>18</sup> Therefore, after a proper conversion, a constant count rate at high energies, assumed by W06 would correspond to a sharply rising physical flux in photons/(s  $\cdot$  cm<sup>2</sup>), which is of course incorrect. We performed a full data analysis, taking into account the dependence of the effective area on the energy and our constraints weakened sharply at high energies. This effect is well-known and is present in many papers that perform spectral analysis of *XMM-Newton* or *Chandra* data.

Our final constraints are shown in Fig. 10. At masses  $m_s \gtrsim$

<sup>18</sup> For PN camera this happens at  $\sim 12$  keV (c.f. Fig. 8).

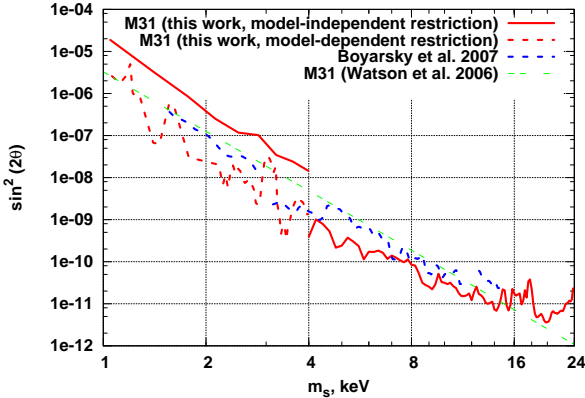


**Figure 10.** Restrictions on  $(m_s, \sin^2(2\theta))$  plane. The strongest previous limits of Boyarsky et al. (2007) as well as results of W06 are shown for comparison. The region *above* the curve is excluded.

4 keV (energies  $E_\gamma \geq 2$  keV) we use the results of statistical constraints from the ring5–13 region. To produce the final restriction, we choose, for each value of  $m_s$ , the *minimal* value of  $\sin^2(2\theta)$ . For  $m_s < 4$  keV ( $E_\gamma < 2$  keV) we plot both the model-independent (full flux) and the model-dependent constraints. The restrictions of Boyarsky et al. (2007) and Watson et al. (2006) are shown for comparison.

The high-energy behaviour of our final statistical constraints differs from that of in Fig. 9. There are several reasons for this. Firstly, in Fig. 9 we showed the full flux restrictions from the MOS camera (to compare our results with those of W06), while in Fig. 10 we used the combined constraints from both MOS and PN cameras. The PN camera has a wider energy range: its effective area decreases only above  $E \approx 10$  keV<sup>19</sup>, which explains the weakening of constraints on Fig.10 for  $m_s \gtrsim 20$  keV. The “peak” at  $m_s \approx 16 - 18$  keV, is due to the presence of strong Cu instrumental lines in the PN background spectrum (Strüder et al. 2001, see also Fig. 8). This region has, thus, higher errors, which weaken the constraints. Finally, we used several jointly fitted spectra (up to 9 in MOSPN-OOT dataset) in our “statistical” method, as opposed to the restrictions in Fig.9 where we used only one spectrum. The combination of several spectra improves the bounds, as statistical errors decrease.

## 6 RESULTS AND CONCLUSIONS

Using available *XMM-Newton* data on the central region of the Andromeda galaxy (M31), we obtained new restrictions on sterile neutrino Dark Matter parameters. We analyzed various DM distributions for the central part of M31, and obtained a conservative estimate of the DM mass inside the central 13′, using the model M31B of Widrow & Dubinski (2005). This DM distribution turned out to be the most conservative among those which studied the DM distribution in the inner part of M31.<sup>20</sup>

<sup>19</sup> *XMM-Newton* Users Handbook, Sec. 3.2.2.1, [http://xmm.esac.esa.int/external/xmm\\_user\\_support/documentation/](http://xmm.esac.esa.int/external/xmm_user_support/documentation/)

<sup>20</sup> We would like to notice, however, that in the work Kerins (2004), a number of “extreme” (i.e. maximizing contributions of disk, spheroid or halo) models are considered. Some of these models would reduce an estimated DM signal from the inner 13′ (and correspondingly our limits) by a factor

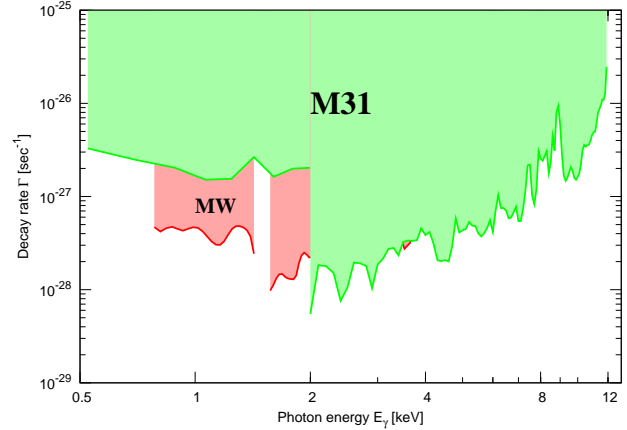


**Figure 11.** Constraints on the decay width  $\Gamma$  of any radiatively decaying DM from this work (marked “M31”) and Boyarsky et al. (2007) (marked “MW”). The shaded region of parameters is excluded.

We found that exclusion of numerous point sources from the central part significantly improves our limits, therefore we have also calculated the DM mass in such “cheesed” regions with the help of Monte Carlo integration.

As the surface brightness is low in the selected regions, the choice of the background subtraction method is important. We processed *XMM-Newton* data from these regions with the help of two different background subtraction techniques – the Extended Sources Analysis Software (ESAS), and the blank-sky background subtraction (SBS), using the blank-sky background dataset of Read & Ponman (2003). We have shown that these totally different background subtraction methods give similar results.

To compare our results with the previous work on M31 (Watson et al. 2006, **W06**), we obtained the full flux restriction from the central 5′ of M31. Our full flux results (shown in Fig. 9) mostly reproduce the results of W06, up to differences arising from our more conservative estimate of expected DM signal and proper data analysis (see Sec. 5.3 for detailed discussion).

Our final upper limits (both model-dependent and model-independent) are shown in Fig. 10. We improved the previous bounds of W06 on  $\sin^2(2\theta)$  by as much as an order of magnitude for masses  $4 \text{ keV} \lesssim m_s \lesssim 8 \text{ keV}$ . Due to the significant low-energy thermal component in M31 diffuse emission, to produce the model-independent constraints, we have used the “full flux” method for  $m_s < 4.0$  keV (i.e.  $E_\gamma < 2.0$  keV). In this region, the strongest constraints remain those of Boyarsky et al. (2007). We have also produced model-dependent constraints for  $E_\gamma < 2.0$  keV, using the “statistical” method; in this case we found the best-fit model by fixing the metallic abundances at the level of optical observations.

The comparison of our upper limit with the lower bound on sterile neutrino pulsar kick mechanism (Fuller et al. 2003) improves the previous bounds and can exclude part of the parameter region (for  $4 \text{ keV} < m_s < 20 \text{ keV}$ ).

Finally, it should be noticed that although throughout this paper we were writing about the sterile neutrino DM, the results of

we chose to use the family of models, shown on Fig. 2, as they qualitatively agree with each other and do not contain any “extreme” assumptions. However, below, in deriving a model-dependent upper limit of the mass of the DM particle, we will introduce an additional penalty factor, to account for this and other possible systematic uncertainties.

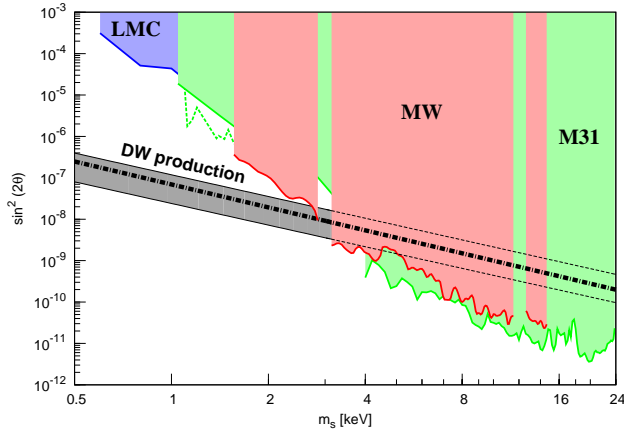


**Figure 12.** Current X-ray constraints, combined with the DW production model. Colored regions are excluded. The grey region shows the range of parameters which give correct abundance in the DW model (Asaka et al. 2007). The color shaded regions mark the restrictions from “LMC” (Boyarsky et al. 2006d), “MW” (Boyarsky et al. 2007) and “M31” (this work). Model-dependent restrictions from M31 for  $m_s < 2$  keV are shown in (green) dashed line.

this work are equally applicable to *any* decaying DM candidate (e.g. gravitino), emitting photon of energy  $E_\gamma$  and having decay width  $\Gamma$ . Our final results in this case are presented in Fig. 11. For other works discussing cosmological and astrophysical effects of decaying DM see de Rujula & Glashow (1980); Berezhiani et al. (1987); Doroshkevich et al. (1989); Berezhiani et al. (1990); Berezhiani & Khlopov (1990). An extensive review of the results can also be found in the book by Khlopov (1997).

### 6.1 Sterile neutrino in Dodelson-Widrow model

The results of this work have important consequences to one of the production models for the sterile neutrino, the so-called “Dodelson-Widrow” (DW) scenario – production through (non-resonant) oscillations with an active neutrino (Dodelson & Widrow 1994). The computation of the abundance is complicated in this case by the fact that the production mainly happens around the QCD transition and therefore QCD contributions are hard to compute (see Asaka et al. 2006, and refs. therein). A first-principles computation, taking into account all QCD contributions in a proper way, was performed in Asaka et al. (2007).

We compare the results of this computation with X-ray bounds obtained in this work and previous works in Fig. 12. The upper and lower dashed lines, bounding the grey area, correspond to the DW production scenario when all hadronic uncertainties are pushed in one or another direction; the thick central line corresponds to the most probable relation between  $m_s$  and  $\sin^2(2\theta)$ . Upon comparison with X-ray bounds, we find that the upper bound on the DM mass in the DW scenario is reliably below  $m_s < 4$  keV (even if we push our X-ray bounds up by a factor of 2, to account for some yet unknown systematics and push all the uncertainties in hadronic contributions to the DW production in one direction).

This improves by 50% the previous bound  $m_s < 6$  keV of Asaka et al. (2007). Notice that other bounds on  $m_s$ , that appeared in the literature (e.g.  $m_s < 3.5$  keV of Watson et al. (2006) and  $m_s < 3$  keV of Boyarsky et al. (2006d)) were based on the computations of Abazajian (2006), which did not take into account all QCD contributions.

Our present results may be combined with the Lyman- $\alpha$  analysis of Seljak et al. (2006); Viel et al. (2006); Viel et al. (2007). As follows from the most recent analysis of Viel et al. (2007), if one uses only the high-resolution high-redshift Lyman- $\alpha$  spectra of Becker et al. (2007) then one finds the lower bound on the sterile neutrino DM mass in the DW scenario to be  $m_s > 5.6$  keV, which is in contradiction with our current upper bound  $m_s < 4$  keV (but would have left a narrow allowed window for  $m_s$  if one had used the previous bound  $m_s < 6$  keV of Asaka et al. 2007). If one takes into account the low-resolution SDSS Lyman- $\alpha$  dataset (McDonald et al. 2006), used in Seljak et al. (2006); Viel et al. (2006), this contradiction becomes much stronger. Although the Lyman- $\alpha$  method relies on a very complicated analysis with (???) some unknown systematic uncertainties, it seems that the model in which all of the DM is produced through the DW scenario is ruled out.

However, there is another way to produce the sterile neutrino through oscillations with active neutrinos (resonant production in the presence of lepton asymmetries, Shi & Fuller 1999 (SF)). In this case, one qualitatively expects that the results of the Lyman- $\alpha$  analysis can be lowered by a significant amount, as for the same mass, the mean velocity (free-streaming length) in the SF model can be much lower than in the DW model. However, as sterile neutrinos are produced in the non-equilibrium way and their spectrum differs significantly from the thermal one, the actual Lyman- $\alpha$  bounds may depend not only on the free-streaming but also on the detailed shape of the spectrum. The detailed analysis of the SF production and corresponding re-analysis of the Lyman- $\alpha$  data is needed. Currently, the SF mechanism is not ruled out.

Finally, there is also the possibility of production of the sterile neutrino DM through the decay of the light inflaton (Shaposhnikov & Tkachev 2006), which cannot be ruled out by X-ray observations.

Therefore, the sterile neutrino remains a viable and interesting DM candidate, which can be either warm or cold. One of the most interesting ranges of parameters is that of low masses, which is also in the potential reach of laboratory experiments (Bezrukov & Shaposhnikov 2007) and will be probed with future X-ray spectrometers (Boyarsky et al. 2006a; den Herder et al. 2007).<sup>21</sup> However, the search for the sterile neutrino DM signal in all energy ranges above Tremaine-Gunn limit should also be conducted.

### ACKNOWLEDGEMENTS

We would like to thank B. Gripcios, A. Neronov, J. Nevalainen, M. Markevich, M. Shaposhnikov, C. Watson for useful comments. D.I. is grateful to ESAC team and especially to M. Kirsch, for granting his stay at ESAC and for useful discussions. D.I. and V.S. are also grateful to M. Ehle, R. Saxton and S. Snowden for useful discussions about ESAS software, to Scientific and Educational Centre<sup>22</sup> of the Bogolyubov Institute for Theoretical Physics in Kiev, Ukraine, and especially to V. Shadura, for creating wonderful atmosphere for young Ukrainian scientists, and to Ukrainian Virtual Roentgen and Gamma-Ray Observatory VIRGO.UA<sup>23</sup> and computing cluster of Bogolyubov Institute for Theoretical Physics<sup>24</sup>, for using their computing resources. This work was supported by the Swiss National Science Foundation and

<sup>21</sup> See also EDGE Project: <http://projects.iasf-roma.inaf.it/edge>

<sup>22</sup> <http://sec.bitp.kiev.ua>

<sup>23</sup> <http://virgo.bitp.kiev.ua>

<sup>24</sup> <http://grid.bitp.kiev.ua>

the Swiss Agency for Development and Cooperation in the framework of the programme SCOPES - Scientific co-operation between Eastern Europe and Switzerland. D.I. also acknowledges support from the INTAS project No. 05-1000008-7865. The work of A.B. was (partially) supported by the EU 6th Framework Marie Curie Research and Training network "UniverseNet" (MRTN-CT-2006-035863). O.R. would like to acknowledge support of the Swiss Science Foundation.

## REFERENCES

- Abazajian, K. 2006, *Phys. Rev.*, D73, 063506, astro-ph/0511630
- Abazajian, K., Fuller, G. M., & Patel, M. 2001, *Phys. Rev. D*, 64, 023501, astro-ph/0101524
- Abazajian, K. N., Markevitch, M., Koushiappas, S. M., & Hickox, R. C. 2007, *Phys. Rev. D*, 75, 063511, ADS, arXiv:astro-ph/0611144
- Alcock, C., et al. 2000, *ApJ*, 541, 270, ADS
- Arnaud, K. A. 1996, in *A.S.P. Conference Serie*, Vol. 101, *Astronomical Data Analysis Software and Systems V*, ed. G. H. Jacoby & J. Barnes (San Francisco, ASP), 17
- Asaka, T., Blanchet, S., & Shaposhnikov, M. 2005, *Phys. Lett.*, B631, 151, hep-ph/0503065
- Asaka, T., Laine, M., & Shaposhnikov, M. 2006, *JHEP*, 06, 053, hep-ph/0605209
- . 2007, *JHEP*, 01, 091, hep-ph/0612182
- Asaka, T., & Shaposhnikov, M. 2005, *Phys. Lett.*, B620, 17, hep-ph/0505013
- Avila-Reese, V., Colín, P., Valenzuela, O., D'Onghia, E., & Firmani, C. 2001, *ApJ*, 559, 516, ADS, arXiv:astro-ph/0010525
- Baltz, E. A., & Murayama, H. 2003, *JHEP*, 5, 67, ADS, arXiv:astro-ph/0108172
- Barger, V. D., Phillips, R. J. N., & Sarkar, S. 1995, *Phys. Lett.*, B352, 365, hep-ph/9503295
- Becker, G. D., Rauch, M., & Sargent, W. L. W. 2007, *ApJ*, 662, 72, ADS, arXiv:astro-ph/0607633
- Bereziani, Z. G., & Khlopov, M. Y. 1990, *Sov. J. Nucl. Phys.*, 52, 60
- Bereziani, Z. G., Vysotsky, M. I., & Khlopov, M. Y. 1987, *Sov. J. Nucl. Phys.*, 45, 1065
- Bereziani, Z. G., Vysotsky, M. I., Yurov, V. P., Doroshkevich, A. G., & Khlopov, M. Y. 1990, *Sov. J. Nucl. Phys.*, 51, 1020
- Bezrukov, F., & Shaposhnikov, M. 2007, *Phys. Rev. D*, 75, 053005, ADS, arXiv:hep-ph/0611352
- Biermann, P. L., & Kusenko, A. 2006, *Phys. Rev. Lett.*, 96, 091301, astro-ph/0601004
- Bisnovatyi-Kogan, G. S. 1980, *AZh*, 57, 899, ADS
- Blair, W. P., Kirshner, R. P., & Chevalier, R. A. 1982, *ApJ*, 254, 50, ADS
- Bode, P., Ostriker, J. P., & Turok, N. 2001, *ApJ*, 556, 93, astro-ph/0010389
- Bond, J. R., Efstathiou, G., & Silk, J. 1980, *Phys. Rev. Lett.*, 45, 1980, ADS
- Bond, J. R., & Szalay, A. S. 1983, *ApJ*, 274, 443, ADS
- Boyarsky, A., den Herder, J. W., Neronov, A., & Ruchayskiy, O. 2006a, To appear in *Astropart. Phys.*, ADS, astro-ph/0612219
- Boyarsky, A., Neronov, A., Ruchayskiy, O., & Shaposhnikov, M. 2006b, *MNRAS*, 370, 213, ADS, astro-ph/0512509
- . 2006c, *Phys. Rev. D*, 74, 103506, astro-ph/0603368
- Boyarsky, A., Neronov, A., Ruchayskiy, O., Shaposhnikov, M., & Tkachev, I. 2006d, *Phys. Rev. Lett.*, 97, 261302, astro-ph/0603660
- Boyarsky, A., Nevalainen, J., & Ruchayskiy, O. 2007, *A&A*, 471, 51, ADS, astro-ph/0610961
- Boyarsky, A., Ruchayskiy, O., & Markevitch, M. 2008, *ApJ*, 673, 752, ADS, astro-ph/0611168
- Burkert, A. 1995, *ApJ*, 447, L25+, ADS, arXiv:astro-ph/9504041
- Carignan, C., Chemin, L., Huchtmeier, W. K., & Lockman, F. J. 2006, *ApJ*, 641, L109, astro-ph/0603143
- Cembranos, J. A. R., Feng, J. L., Rajaraman, A., Smith, B. T., & Takayama, F. 2006, ADS, hep-ph/0603067
- Dalcanton, J. J., & Hogan, C. J. 2001, *ApJ*, 561, 35, astro-ph/0004381
- Dar, A. 1995, *ApJ*, 449, 550, ADS, arXiv:astro-ph/9504082
- de Rujula, A., & Glashow, S. L. 1980, *Phys. Rev. Lett.*, 45, 942, ADS
- den Herder, J. W., et al. 2007, in *Proc. SPIE*, Vol. 6688, 4
- Dennefeld, M., & Kunth, D. 1981, *AJ*, 86, 989, ADS
- Diemand, J., Kuhlen, M., & Madau, P. 2007, *ApJ*, 657, 262, ADS, astro-ph/0611370
- Dodelson, S., & Widrow, L. M. 1994, *Phys. Rev. Lett.*, 72, 17, hep-ph/9303287
- Dolgov, A. D., & Hansen, S. H. 2002, *Astropart. Phys.*, 16, 339, hep-ph/0009083
- Doroshkevich, A. G., Khlopov, M. I., & Klypin, A. A. 1989, *MNRAS*, 239, 923, ADS
- Doroshkevich, A. G., Khlopov, M. I., Sunyaev, R. A., Szalay, A. S., & Zeldovich, I. B. 1981, *New York Academy Sciences Annals*, 375, 32, ADS
- Einasto, J. et al. 1974, *Tartu Astrofüüsika Observatoorium Teated*, 48, 3, ADS
- Fogli, G. L., Lisi, E., Marrone, A., Palazzo, A., & Rotunno, A. M. 2006, *Prog. Part. Nucl. Phys.*, 57, 71, ADS, arXiv:hep-ph/0506083
- Fuller, G. M., Kusenko, A., Mocioiu, I., & Pascoli, S. 2003, *Phys. Rev.*, D68, 103002, astro-ph/0307267
- Gates, E. I., Gyuk, G., & Turner, M. S. 1995, *ApJ*, 449, L123+, ADS, astro-ph/9505039
- Geehan, J. J., Fardal, M. A., Babul, A., & Guhathakurta, P. 2006, *MNRAS*, 366, 996, ADS, arXiv:astro-ph/0501240
- Ghigna, S., Moore, B., Governato, F., Lake, G., Quinn, T., & Stadel, J. 2000, *ApJ*, 544, 616, ADS, astro-ph/9910166
- Gilmore, G. 2007, ADS, astro-ph/0703370
- Gilmore, G., Wilkinson, M., Kleyna, J., Koch, A., Wyn Evans, N., Wyse, R. F. G., & Grebel, E. K. 2006, ADS, astro-ph/0608528
- Gilmore, G., Wilkinson, M. I., Wyse, R. F. G., Kleyna, J. T., Koch, A., Evans, N. W., & Grebel, E. K. 2007, *ApJ*, 663, 948, ADS, arXiv:astro-ph/0703308
- Giunti, C. 2007, *Nucl. Phys. Proc. Suppl.*, 169, 309, hep-ph/0611125
- Goerdt, T., Moore, B., Read, J. I., Stadel, J., & Zemp, M. 2006, *MNRAS*, 368, 1073, ADS, astro-ph/0601404
- Hidaka, J., & Fuller, G. M. 2006, *Phys. Rev. D*, 74, 125015, ADS, astro-ph/0609425
- Hidaka, J., & Fuller, G. M. 2007, 706, ADS, 0706.3886
- Hui, L., Gnedin, N. Y., & Zhang, Y. 1997, *ApJ*, 486, 599, ADS, astro-ph/9608157
- Jacoby, G. H., & Ciardullo, R. 1999, *ApJ*, 515, 169, ADS, arXiv:astro-ph/9812165
- Jacoby, G. H., & Ford, H. C. 1986, *ApJ*, 304, 490, ADS
- Jansen, F. et al. 2001, *A&A*, 365, L1
- Kerins, E., et al. 2001, *MNRAS*, 323, 13, ADS,

- arXiv:astro-ph/0002256
- Kerins, E. 2004, MNRAS, 347, 1033, ADS, arXiv:astro-ph/0310537
- Khlopov, M. Y. 1997, *Cosmoparticle Physics* (World Scientific Pub Co Inc)
- King, I. 1962, AJ, 67, 471, ADS
- Kleyna, J. T., Wilkinson, M. I., Gilmore, G., & Evans, N. W. 2003a, ApJ, 588, L21, ADS, astro-ph/0304093
- . 2003b, ApJ, 589, L59, ADS
- Klypin, A., Kravtsov, A. V., Valenzuela, O., & Prada, F. 1999, ApJ, 522, 82, ADS, arXiv:astro-ph/9901240
- Klypin, A., Zhao, H., & Somerville, R. S. 2002, ApJ, 573, 597, ADS, astro-ph/0110390
- Koposov, S. et al. 2007, ApJ, 663, 948, ADS, 0706.2687
- Kusenko, A. 2006, Phys. Rev. Lett., 97, 241301, hep-ph/0609081
- Lasserre, T., et al. 2000, A&A, 355, L39, ADS, arXiv:astro-ph/0002253
- Liedahl, D. A., Osterheld, A. L., & Goldstein, W. H. 1995, ApJ, 438, L115, ADS
- McDonald, P. et al. 2006, ApJS, 163, 80, ADS, arXiv:astro-ph/0405013
- Mewe, R., Lemen, J. R., & van den Oord, G. H. J. 1986, A&AS, 65, 511, ADS
- Miranda, M., & Macciò, A. V. 2007, 706, ADS, 0706.0896
- Moore, B., Quinn, T., Governato, F., Stadel, J., & Lake, G. 1999, MNRAS, 310, 1147, ADS, astro-ph/9903164
- Morrison, R., & McCammon, D. 1983, ApJ, 270, 119, ADS
- Navarro, J. F., Frenk, C. S., & White, S. D. M. 1997, ApJ, 490, 493, astro-ph/9611107
- Navarro, J. F. et al. 2004, MNRAS, 349, 1039, ADS, arXiv:astro-ph/0311231
- Nevalainen, J., Markevitch, M., & Lumb, D. 2005, ApJ, 629, 172, astro-ph/0504362
- Pal, P. B., & Wolfenstein, L. 1982, Phys. Rev., D25, 766
- Palazzo, A., Cumberbatch, D., Slosar, A., & Silk, J. 2007, arXiv:0707.1495 [astro-ph]
- Peebles, P. J. E. 1980, *The large-scale structure of the universe* (Princeton, N.J., Princeton University Press, 1980. 435 p.), ADS
- . 1984, Science, 224, 1385, ADS
- Penarrubia, J., McConnachie, A., & Navarro, J. F. 2007, ADS, astro-ph/0701780
- Read, A. M., & Ponman, T. J. 2003, A&A, 409, 395, ADS, astro-ph/0304147
- Riemer-Sørensen, S., Hansen, S. H., & Pedersen, K. 2006, ApJ, 644, L33, ADS, astro-ph/0603661
- Ruchayskiy, O. 2007, in *Proceedings of the 11th Marcel Grossmann Meeting on General Relativity*, ed. H. Kleinert, R. Jantzen, & R. Ruffini (World Scientific), arXiv:0704.3215 [astro-ph]
- Sánchez-Salcedo, F. J., Reyes-Iturbide, J., & Hernandez, X. 2006, MNRAS, 370, 1829, ADS, arXiv:astro-ph/0601490
- Seljak, U., Makarov, A., McDonald, P., & Trac, H. 2006, Phys. Rev. Lett., 97, 191303, astro-ph/0602430
- Seto, O., & Yamaguchi, M. 2007, Phys. Rev. D, 75, 123506, ADS, arXiv:0704.0510
- Shaposhnikov, M., & Tkachev, I. 2006, Phys. Lett., B639, 414, hep-ph/0604236
- Shi, X.-d., & Fuller, G. M. 1999, Phys. Rev. Lett., 82, 2832, astro-ph/9810076
- Shirey, R. et al. 2001, A&A, 365, L195, ADS, arXiv:astro-ph/0011244
- Simon, J. D., & Geha, M. 2007, 706, ADS, 0706.0516
- Smith, R. K., Brickhouse, N. S., Liedahl, D. A., & Raymond, J. C. 2001, ApJ, 556, L91, ADS, arXiv:astro-ph/0106478
- Sommer-Larsen, J., & Dolgov, A. 2001, ApJ, 551, 608, ADS, arXiv:astro-ph/9912166
- Stanek, K. Z., & Garnavich, P. M. 1998, ApJ, 503, L131+, ADS, arXiv:astro-ph/9802121
- Stasielak, J., Biermann, P. L., & Kusenko, A. 2007, ApJ, 654, 290, ADS, arXiv:astro-ph/0606435
- Strigari, L. E., Bullock, J. S., Kaplinghat, M., Diemand, J., Kuhlen, M., & Madau, P. 2007, 704, ADS, 0704.1817
- Strüder, L. et al. 2001, A&A, 365, L18
- Strumia, A., & Vissani, F. 2006, hep-ph/0606054
- Takahashi, H., Okada, Y., Kokubun, M., & Makishima, K. 2004, ApJ, 615, 242, ADS, arXiv:astro-ph/0408305
- Tegmark, M., et al. 2004, Phys. Rev., D69, 103501, astro-ph/0310723
- Tempel, E., Tamm, A., & Tenjes, P. 2007, 707, ADS, 0707.4374
- Tremaine, S., & Gunn, J. E. 1979, Phys. Rev. Lett., 42, 407
- Turner, M. J. L. et al. 2001, A&A, 365, L27, arXiv:astro-ph/0011498
- Viel, M., Becker, G. D., Bolton, J. S., Haehnelt, M. G., Rauch, M., & Sargent, W. L. W. 2007, 709, ADS, 0709.0131
- Viel, M., Lesgourgues, J., Haehnelt, M. G., Matarrese, S., & Riotto, A. 2006, Phys. Rev. Lett., 97, 071301, astro-ph/0605706
- Watson, C. R., Beacom, J. F., Yuksel, H., & Walker, T. P. 2006, Phys. Rev., D74, 033009, astro-ph/0605424
- White, S. D. M., Frenk, C. S., & Davis, M. 1983, ApJ, 274, L1, ADS
- Widrow, L. M., & Dubinski, J. 2005, ApJ, 631, 838, ADS, arXiv:astro-ph/0506177
- Wu, X. 2007, ADS, astro-ph/0702233
- Zel'dovich, Y. B. 1970, A&A, 5, 84, ADS